

# Supporting Information for

## **Doping-Induced Tunable Wettability and Adhesion of Graphene**

Ali Ashraf<sup>1</sup>, Yanbin Wu<sup>1</sup>, Michael Cai Wang<sup>1</sup>, Keong Yong<sup>1</sup>, Tao Sun<sup>1</sup>, Yuhang Jing<sup>1</sup>,  
Richard T. Haasch<sup>2</sup>, Narayana R. Aluru<sup>1</sup>, SungWoo Nam<sup>1,\*</sup>

<sup>1</sup>Department of Mechanical Science and Engineering, University of Illinois at Urbana-Champaign, Urbana, Illinois 61801, United States.

<sup>2</sup>Frederick Seitz Materials Research Laboratory, University of Illinois at Urbana-Champaign, Urbana, Illinois 61801, United States.

Correspondence to: [swnam@illinois.edu](mailto:swnam@illinois.edu)

### Table of Contents:

1. Methods
2. Considerations during WCA Measurements
3. Measurement of Doping Level
4. Graphene Layer Thickness and Roughness Measurements
5. Comparison of Surface Functional Groups
6. WCA Modulation by Band Bending and Metal Doping
7. Considerations during Adhesion Force Measurement
8. Analytical Model for WCA Modulation by Doping
9. Supporting Figures S1-S21
10. Supporting References

## 1. Methods

### a) Graphene Growth by Chemical Vapor Deposition (CVD)

A 25- $\mu\text{m}$ -thick copper foil (Alfa Aesar, MA) of a suitable size (2" by 2") was cleaned by rinsing with acetone, isopropyl alcohol (IPA), and deionized (DI) water as a pretreatment step. The air-dried copper foil was used for graphene growth via a standard CVD method (Rocky Mountain Vacuum Tech, Inc., CO). The detailed procedure was discussed in an earlier study<sup>1</sup>. Briefly, a pretreated copper foil was annealed under hydrogen ( $\text{H}_2$ ) at 1050°C for 30 min. During the growth stage, methane gas was used as a carbon precursor along with  $\text{H}_2$  for 2 min. Subsequently, using a load lock, the as-grown graphene sample was rapidly cooled under an argon (Ar) atmosphere. The backside graphene was removed with 500-W oxygen plasma (Diener GmbH, Germany) for 40 sec while protecting the topside graphene on the copper foil with a poly(methyl methacrylate) (PMMA) (Sigma Aldrich, MO) film (spun at 3000 rpm for 30 sec). The PMMA film was then dissolved in acetone (kept in solvent for at least 10 min) to obtain copper foil with a graphene film on only one side.

### b) Chemical Doping of Graphene

To dope graphene with a subsurface polyelectrolyte, the graphene was transferred onto a polyelectrolyte-coated silicon dioxide ( $\text{SiO}_2$ ) on silicon (Si) wafer. Because the polyelectrolytes are not compatible with the organic solvents used to remove the polymeric scaffolds (e.g., PMMA) via the conventional solution-transfer process, a polymer-free transfer method was implemented similar to that described in an earlier study<sup>1</sup>. However, instead of manually transferring the graphene from the liquid bath to the substrate of interest, we lowered the graphene by draining the liquid in the container to reveal the pre-placed substrate. This preserves the water-soluble polyelectrolyte layer coated onto the  $\text{SiO}_2/\text{Si}$ .

Our transfer method has the advantage of semiautomatic operation and enables the direct transfer of graphene in a polyelectrolyte-rich solution (Fig. S1). This transfer method involves injecting copper etchant solution underneath a copper foil with a peristaltic pump (Cole Parmer, IL). After complete etching of the copper foil, the etchant solution was replaced with DI water at a 5:1 (v:v) ratio to the etchant solution to clean the free-floating graphene sample. Then, the polyelectrolyte solution was injected into DI water (the concentration varied for the different polyelectrolytes). The different polyelectrolytes (Sigma Aldrich, MO) used for this investigation were high molecular weight (HMW) poly (allylamine hydrochloride) (PAH) (MW ~450,000), poly (styrene sulfonate) (PSS) (MW ~1,000,000), poly-L-lysine (PLL) (MW ~150,000-300,000), and poly (acrylic acid) (PAA) (MW ~450,000). After soaking the  $\text{SiO}_2/\text{Si}$  substrate in a polyelectrolyte solution for at least 15 min, the polyelectrolyte-rich solution was removed using the pump to lower and place the graphene on top of the  $\text{SiO}_2/\text{Si}$  substrate, trapping polyelectrolyte solution between the graphene and the  $\text{SiO}_2/\text{Si}$  substrate. As the floating graphene layer was hydrophobic because of airborne contaminants<sup>2</sup>, the hydrophilic polyelectrolyte solution had minimal tendency to spill over the graphene layer during the transfer process. Therefore, the top side of the polyelectrolyte-doped graphene sample was free of polyelectrolyte contamination, as confirmed by environmental scanning electron microscopy (E-SEM) during the water contact angle (WCA) measurement. The chemically

doped samples produced in this manner were thermally annealed at 100-150 °C (depending on the polyelectrolyte melting temperature) for 45-60 min in Ar to remove residual moisture. The graphene sample obtained in this manner was effectively doped by the underlying polyelectrolyte layer<sup>3</sup>, as discussed in more detail below.

c) Graphene-Gold Junction Fabrication

The gold (Au) pads (50 nm) were defined by photolithography (MEGAPOSIT SPR220-4.5, MicroChem, MA) and metallized by a thermal evaporator (Nano 36, Kurt J. Lesker, PA) onto a Si wafer with a 300-nm-thick thermal oxide. The graphene was then transferred onto the Au/SiO<sub>2</sub>/Si substrate using the method discussed above, and the samples were annealed under Ar at 150 °C for 1 hr to remove residual moisture.

d) WCA Measurement

E-SEM (FEI quanta 450 & Philips XL 30, OR) was used to condense micrometer-sized water droplets at 100% relative humidity (RH) on cooled (4 °C) graphene samples using a customized beveled sample holder (Fig. S2). Only droplet sizes of 10 micrometer or larger were considered for WCA measurements to eliminate the possibility of droplet shape distortion because of electron beam heating<sup>4</sup>. As graphene is thermally conductive, the chance of electron beam heating-induced droplet shape alteration was minimal.

The E-SEM images were analyzed with ImageJ software (NIH, USA) with a drop-analysis plugin based on fitting the Young–Laplace equation to the images<sup>5,6</sup>. A statistical approach was used to calculate the average WCA with an error bar by analyzing at least 5 different samples of each type and at least 5 regions on each sample. Because of the inhomogeneity and defects of CVD-grown graphene across a few micrometer-size domains<sup>7</sup>, slight variations in the WCA were expected.

Macroscopic WCA measurements were performed with a KSV CAM200 goniometer (KSV Instruments, Ltd., Finland).

e) Spectroscopic Investigation

The X-ray photoelectron spectroscopy (XPS) analysis of doped and undoped graphene samples at grazing (15°) and normal takeoff angles was performed using a Kratos Axis ULTRA instrument (Kratos Analytical, Ltd., UK). The functional group composition was calculated using high-resolution spectra with relative sensitivity factors for carbon and oxygen of 0.278 and 0.711, respectively. A detailed procedure for this investigation was described in an earlier study<sup>2</sup>. The XPS data were analyzed using CasaXPS software (Casa software, Ltd., UK).

Raman spectra were collected with a Renishaw Raman microscope (Renishaw plc, UK) with a 633-nm laser, a 20× objective lens, and a 30-sec acquisition time using inVia WiRE 3.3 software.

Ultraviolet photoelectron spectroscopy (UPS) analysis of doped and undoped graphene samples was performed with a helium II source using a PHI 5400 instrument (Physical Electronics, MN). UPS data were analyzed using CasaXPS software.

f) Atomic Force Microscopy (AFM)-based Investigation

Root mean square (RMS) roughness measurements, graphene layer thickness measurements, adhesion force measurements, and scanning Kelvin probe microscopy

(SKPM) were performed using a Cypher AFM instrument (Asylum Research, CA). The RMS roughness and graphene layer thickness were measured over a 3 by 3  $\mu\text{m}^2$  area using tapping mode (0.5-Hz scan rate) with standard aluminum-coated silicon probes (TAP 300Al-G, BudgetSensors, Bulgaria). SKPM was performed over a 3 by 1  $\mu\text{m}^2$  area using tapping mode (0.5-Hz scan rate) with Cr/Pt coated silicon probes (TAP 300E-G, BudgetSensors, Bulgaria). Gold deposited by thermal evaporator was used as a reference for work function (WF) calculation of SKPM data. Adhesion force measurements were conducted over an 18  $\mu\text{m}^2$  area (128 data points were collected in this area) in contact mode using octadecyltrichlorosilane (OTS) (Sigma-Aldrich, MO)-coated silicon tips with an aluminum reflex coating (Multi 75Al-G, BudgetSensors, Bulgaria). The silicon tips were cleaned by oxygen plasma and coated with dilute OTS (1 mM) using the method reported by Flatter *et al.*<sup>8</sup>.

#### g) Graphene Field Effect Transistor Fabrication and Measurement

Synthesized monolayer graphene by the method described above, was transferred onto a Si wafer with a 300-nm-thick thermal oxide. Graphene channels were patterned with photolithography and oxygen plasma reactive ion etching (Diener GmbH, Germany) for 30 sec (500 W & 150 mTorr). The source/drain electrodes were patterned with photolithography and metallized with Cr/Au (5 nm/ 50 nm) by a thermal evaporator.

The field effect transistor (FET) transfer ( $I$ - $V_{\text{wg}}$ ) characteristics were investigated with a probe station (model PM8, Karl SUSS, Germany) and digital sourcemeter (2614B, Keithley Instruments, OH) using an Ag/AgCl reference electrode (Harvard Instruments, MA) to gate the device through freshly generated DI water, followed by two polyelectrolyte solutions (HMW PSS and PAH). All measurements were performed under ambient conditions.

#### h) First Principles and Atomistic Simulations

Systematic first principles density functional theory (DFT) simulations were conducted using the Vienna Ab Initio Simulation Package (VASP)<sup>9</sup>. We chose generalized gradient approximations (GGA) with the Perdew-Burke-Ernzerhof (PBE) exchange-correlation functional<sup>10</sup>. The projector-augmented wave (PAW) pseudopotentials were employed. The plane-wave basis set was used with an energy cutoff of 500 eV. For the study of graphene doping with polyelectrolytes, we used one monomer of the polyelectrolytes to study the doping effect. Four different configurations of monomers with respect to graphene were considered. A 7 $\times$ 8 unit cell of graphene was used. The Brillouin zone was sampled with 4 $\times$ 4 $\times$ 1 Gamma-centered grids for structural relaxation and 16 $\times$ 16 $\times$ 1 grids for calculating the WF. A vacuum region of 20 Å was applied in the z-direction of the periodic box to avoid nonphysical effects from images. The structures were relaxed until the maximum residual force was less than 0.05 eV/Å before calculating WFs. The systems of doped graphene have dopants only on one side of the graphene, giving rise to a non-symmetric surface with a net electric dipole moment. We added a dipole correction<sup>11</sup> to cancel out the fake electric field arising from dipole interactions with images.

The random phase approximation (RPA) calculations were performed using the VASP package, PAW potentials, spin polarization, and an energy cutoff of 408 eV. The response function was expanded in plane waves up to an energy cutoff of 272 eV. We

checked the basis set convergence by increasing the plane wave cutoff to 600 eV and the response function cutoff to 400 eV and found negligible change ( $<1$  meV). The exchange energy and correlation energy were computed with an identical  $2 \times 2$  supercell size and a  $8 \times 8 \times 1$  Monkhorst-Pack k-mesh for sampling the Brillouin zone<sup>12,13</sup>. The long-wavelength contributions are neglected in both the exchange and the correlation energy<sup>13</sup>. A separate exchange energy calculation with an  $8 \times 8$  supercell and a  $2 \times 2 \times 1$  k-mesh was performed to correct the dependence of the exchange energy on the supercell size<sup>12</sup>. A lattice constant of 20 Å along the direction perpendicular to the graphene surface (z-axis) was used. To compute the interaction energy, a system with the water separated from the graphene by 7 Å was used as the zero reference. A single boron or oxygen atom, instead of the polyelectrolyte, was used to dope graphene due to computational limit. The WF was also computed using DFT for the systems with a single atom as the dopant.

The RPA data were used to develop force field parameters for use in molecular dynamics (MD) simulations. The van der Waals (vdW) center of the water molecule was chosen at the M point that coincides with the virtual site of the TIP4P water molecule<sup>14</sup>. Choosing the vdW center at the M point was found to minimize the interaction difference attributed to the water orientation. The parameters were obtained by fitting to the Boltzmann averaged interaction energies among different orientations. A least squares fit was used in the fitting.

The WCA on graphene was simulated using MD simulations. The dimensions of the graphene layer were approximately  $30 \text{ nm} \times 30 \text{ nm}$ , effectively removing the interaction between the droplet and its periodic images. The graphene was fixed throughout the simulation<sup>15</sup>. The simulation box size perpendicular to the graphene surface plane was 20 nm. The MD simulations were performed with the GROMACS 4.5.3 package<sup>16</sup>. Time integration was performed using the leapfrog algorithm<sup>17</sup> with a time step of 2.0 fs. The short-range vdW interactions were computed using a cutoff scheme (cutoff distance, 1.4 nm). The long-range electrostatic interactions were computed using a particle mesh Ewald method (real space cutoff, 1.4 nm; fast Fourier transform [FFT] grid spacing, 0.12 nm, fourth-order interpolation). The Nosé-Hoover thermostat<sup>18,19</sup> with a time constant of 0.5 ps was used to maintain the temperature at 300 K. A water cubic box was initially placed on top of the graphene surface. The system was equilibrated for 6 ns using the *NVT* (constant number [N], volume [V] and temperature [T]) ensemble, during which the water cubic box evolved into a spherical shape. The energy and temperature of the system reached constant values during this equilibration process. The resulting configuration was used as the starting point for further simulations on data collection. To collect sufficient statistics to compute the WCA, the simulations were run for 5 ns.

## 2. Considerations during WCA Measurements

To find the optimum inclination angle for the beveled sample holder, E-SEM was performed at 0°, 20°, 30°, and 45° inclination angles. Because the WCA is the same for all inclination angles (Fig. S3), the angle that produced images with the best contrast and brightness was chosen for the investigations. An inclination angle of 30° was consistently used for all investigations (Fig. S3).

The microscopic areas selected for WCA measurements were observed before and after water droplet formation to verify whether the graphene film was damaged after the contact with water (Fig. S4). On graphene films that are mostly free of defects, spherical water droplets will form (Fig. S4). The Raman spectra before and after the E-SEM investigation were also compared to ascertain that the graphene film remained intact (Fig. S5). A broken graphene film will result in filmwise condensation because of an exposed hydrophilic polyelectrolyte (doped sample)/SiO<sub>2</sub> (undoped sample) surface (Fig. S6) rather than droplet formation on graphene.

Exposed polyelectrolyte under the broken graphene film was found to swell with time during the E-SEM characterization, and no water droplet formed (Fig. S7). Because of this interesting swelling phenomenon, graphene floated and moved during the E-SEM characterizations (Fig. S8). In contrast, intact graphene prevented the swelling of the polyelectrolyte underneath by restricting the flow of water vapor.

Macroscopic WCA measurements did not produce reliable results. Without thermal annealing, the WCA measurements of both the doped and undoped graphene samples revealed the WCA of the underlying SiO<sub>2</sub> substrate instead. The macroscopic WCA measurements of the thermally annealed polyelectrolyte-doped sample varied with time (Fig. S9a), as the graphene film gradually delaminates when in contact with macroscopic water droplets (Fig. S9b).

To prove that the WCA is not influenced by the polymer main chain but instead by the charged groups of the polyelectrolyte, we conducted a control experiment with PMMA. To this end, graphene was transferred onto a PMMA-coated SiO<sub>2</sub>/Si substrate (PMMA is a polymer that has a similar structure to the tested polyelectrolytes but does not include charged groups). The WCA on this sample measured by E-SEM was ~80° (Fig. S11), demonstrating that the charged groups of the polyelectrolyte are required for wettability modulation by doping. Graphene on PMMA was similar to other graphene samples in terms of the number of layers and defects as confirmed by Raman spectrum (Fig. S11b).

## 3. Measurement of Doping Level

In addition to measuring the doping level by SKPM and Raman spectroscopy, as described in the main text, UPS, graphene FET, and simulation investigations were also performed. Using CasaXPS software for curve fitting, the raw UPS data were analyzed to determine the WF of the graphene samples (Fig. S12a). UPS data analysis confirmed that the graphene was successfully doped by the polyelectrolytes (Fig. S12b). Similar to the SKPM and Raman spectroscopy results, UPS revealed that the HMW PAH and PLL n-doped graphene, whereas the HMW PAA and PSS p-doped graphene (Fig. S12b). SiO<sub>2</sub> substrate p-doped graphene in ambient atmosphere because of gaseous dopants (moisture and oxygen), whereas it n-dopes graphene in vacuum<sup>20,21</sup>. Therefore, for the graphene on SiO<sub>2</sub> sample analyzed by UPS under ultra-high vacuum (UHV), the WF measurement indicated n-doping. The doping amount resulting from molecular adsorption from the air

was only significant after annealing at temperatures above 200°C because more adsorption sites become available after annealing at higher temperatures<sup>22</sup>. Thus, for graphene on SiO<sub>2</sub> annealed at 150 °C in an inert atmosphere, the p-doping was relatively low during the E-SEM investigation (at 100% RH)<sup>22,23</sup>. Therefore, for comparison with the strongly doped graphene on the HMW polyelectrolyte samples, the graphene on SiO<sub>2</sub> sample was considered as an undoped graphene sample.

The characterization of the graphene FET's Dirac point in the HMW PAH and PSS solutions was also consistent with the polyelectrolyte-induced doping measured by UPS (Fig. S13). Dirac point shifts in opposite directions during subsequent solution gating by p- and n-doping polyelectrolytes demonstrated the effectiveness of the chosen polyelectrolytes in doping graphene (Fig. S13a). The doping levels determined from the Dirac point shift ( $\Delta V$ ) were -0.19 V for HMW PAH and +0.17 V for HMW PSS (Fig. S13b), which are consistent with the values reported in the literature<sup>3</sup>.

Simulation results also demonstrated that the WF of graphene changed because of chemical doping by the polyelectrolytes (Fig. S14). The graphene WFs were obtained as the difference between the system's vacuum and Fermi levels. The vacuum level could be calculated as the converged average electrostatic potentials in the vertical direction from the graphene surface. Because there were two different vacuum levels, the system had two different WFs corresponding to the two sides of graphene. Because our surface included dopant on only one side, we calculated the WF on the side without dopant for consistency with the experiments. In addition to the WF changes, we calculated the Bader populations<sup>24-27</sup> of the systems and the numbers of electrons transferred to the graphene, as shown in Fig. S14. A positive Bader charge transfer indicates that charge transfers from dopant to graphene, and vice versa. We also calculated the magnitude of graphene doping by water molecules. For four different water molecule orientations, the doping level of graphene was negligible compared to that resulting from strong dopants, such as boron and oxygen, which result in the same levels of doping as HMW polyelectrolytes (Fig. S15). Therefore, the doping resulting from interaction with water molecules was neglected during the WCA calculation by MD simulations. Only strong doping by boron and oxygen, equivalent to HMW polyelectrolyte doping, was considered during the WCA calculation; the results are shown in the main text (Fig. 4).

#### 4. Graphene Layer Thickness and Roughness Measurements

To investigate whether the graphene grown by our CVD method consisted of a single layer or bilayer, we measured the graphene layer thickness using AFM. To ensure that no residual moisture existed between the graphene and the SiO<sub>2</sub>/Si substrate, the sample was further annealed at 300 °C under Ar for 3 hrs. The thickness of the graphene layer on top of the SiO<sub>2</sub>/Si substrate was found to be ~0.35 nm (Fig. S16a). This result, along with the Raman spectroscopy results (Fig. 2 in the main text), confirms that graphene grown by our CVD method is predominantly single-layer graphene.

We also compared the roughness levels of the doped and undoped graphene samples by AFM. The RMS roughnesses of all samples were similar, with values less than 10 nm (Fig. S16b).

## 5. Comparison of Surface Functional Groups

For both the doped and undoped graphene samples, we performed XPS to compare their surface functional groups (Fig. S17a-d). XPS at a normal takeoff angle detects 8-10 atomic layers from the top of the surface<sup>28</sup>. However, this represents a challenge for doped graphene because a significant portion of the analyzed photoelectrons come from the polymeric background of the subsurface polyelectrolyte (Fig. S17c & d). Therefore, to increase the surface sensitivity for the investigation of single-layer graphene (~0.35 nm) transferred onto polyelectrolyte, we performed angle-resolved X-ray photoelectron spectroscopy (ARXPS) (Fig. S17e & f). Our 15° grazing angle ARXPS showed enhanced surface sensitivity (reduced probing depth by  $\sin(15^\circ)$ ) relative to regular XPS and probed only ~3 atomic layers (i.e., ~1 nm)<sup>28</sup>. The airborne contaminant layer on graphene was shown to be approximately 0.5 nm thick<sup>29</sup>. Therefore, a semi-quantitative comparison between doped and undoped graphene samples with strongly adsorbed contaminant layers (1-nm total thickness of single-layer graphene and contaminant layer) is possible using a combination of normal and grazing angle XPS, and using adjustment factors for doped graphene. C1s high-resolution spectra from both doped and undoped graphene samples were analyzed by curve fitting (Figs. S17a, S17c, & S17e). Hydrophobic functional groups (C-H) from the contaminant layer were not considered during these curve fittings. Because the ARXPS of doped graphene showed the presence of C-N bonds (i.e., some photoelectrons from the subsurface polyelectrolyte were detected) (Fig. S17e), the relative amount of hydrophilic groups in the doped graphene was adjusted.

To calculate the adjustment factors and subsequently compare the doped and undoped graphene samples, we used the following methodology. The ARXPS probing depth of ~1 nm was split into three parts: an approximately 0.5-nm contaminant layer, a 0.35-nm graphene layer, and a 0.15-nm polyelectrolyte layer. Therefore, in addition to contributions from the contaminant and graphene layers, which are similar for the doped and undoped graphenes, the doped graphene could also have a contribution of as much as 15% from the polyelectrolyte (from the 0.15-nm polyelectrolyte layer in the probed region) for the C-C bond. Therefore, for comparison, the C-C bond percentage of the doped graphene was reduced by 15%. Because the polyelectrolyte does not contain any chemical bonds with oxygen, hydrophilic groups were present only on the graphene surface and the contaminant layer. Therefore, the percentage of hydrophilic groups was also adjusted. For a fair comparison, the hydrophilic group compositions of the doped graphene sample were adjusted by a factor of  $\frac{100}{85}$ , or 1.176, to obtain their true percentages. For example, the adjusted C-O/C-C for the doped sample was calculated as

$$\frac{C - O}{C - C} = \frac{3.64 * \textit{adjustment factor for hydrophilic groups}}{91.18 * \textit{adjustment factor for C - C bond}} = \frac{3.64 * 1.176}{91.18 * 0.85} = 0.056$$

The comparison between the doped and undoped graphenes is presented in the main text. For this comparison, the ratio between the oxygen-containing functional groups and C-C bond percentages was calculated using the adjustment factors for the doped graphene sample only.

## 6. WCA Modulation by Band Bending and Metal Doping

The WCA changed with the distance from the graphene-gold junction because of the band bending-induced surface potential modulation of graphene (Fig. S18a). The water droplet spread more (WCA  $\sim 70^\circ$ ) near the graphene-gold junction as a result of the change in graphene's WF (i.e., doping). As the water droplet moved away from the junction, the WCA gradually became larger and finally achieved the WCA value for graphene on SiO<sub>2</sub> without any graphene-gold junction ( $75^\circ$  at 50  $\mu\text{m}$  and  $78^\circ$  at approximately 70  $\mu\text{m}$ ). The Raman spectra at different distances from the junction showed no observable change in graphene quality, demonstrating that the graphene was not damaged during the transfer process onto gold (Fig. S18b). A  $\sim 30\text{-meV}$  drop in the graphene surface potential with a sharp peak was observed near the junction (Fig. S18c and S18d), which is consistent with previously published results<sup>30</sup>. A gradual change in the surface potential from 690 meV to 740 meV occurred over a distance of 40 microns after the sharp peak near the junction and could not be captured in one graph because of the scan size limit of the specific SKPM instrument used.

Graphene sitting on top of a metal is known to become doped by the metal<sup>31–33</sup>. The amount and type of doping depend on the type of metal. We investigated the WCA modulation of graphene grown on a polycrystalline copper foil and graphene transferred onto a gold pad. Graphene is weakly n-doped by copper ( $\sim 0.10\text{ eV}$ ) and relatively strongly p-doped by gold ( $\sim 0.25\text{ eV}$ )<sup>33</sup>. Our investigation showed that the average WCA of graphene on copper is similar to that of nominally undoped graphene on SiO<sub>2</sub> ( $78^\circ$ ), whereas graphene on gold showed a WCA of  $76^\circ$  (Fig. S19). Interestingly, for the even stronger p-doping of graphene by platinum (Pt), Amadei *et al.* reported a value that was  $4^\circ$  smaller than that of graphene on gold<sup>34</sup>. Future investigations of subsurface metals that can cause stronger doping could shed more light on this phenomenon.

## 7. Considerations during Adhesion Force Measurement

Because the non-specific binding of OTS may occur during the OTS treatment of an AFM probe tip made with any material other than silicon, the results obtained using those tips are not reliable as the coating may be partially or totally removed during measurement as a result of weak bonding. Therefore, OTS-coated silicon probe tips with a backside aluminum reflex coating were used for all measurements. The aluminum reflex coating prevents fluctuation in the collected signal by reflecting the light coming from the deflection sensor. To ensure that the variation in the adhesion force was attributable to the interaction of graphene with the OTS layer, a control experiment was designed involving a bare silicon tip with a backside aluminum reflex coating. There was no difference between the adhesion forces of hydrophobic graphene and hydrophilic SiO<sub>2</sub> during the control test with the uncoated AFM probe (Fig. S20). Thus, the adhesion force measurement results presented in the main text reflected the interaction between doped/undoped graphene and hydrophobic OTS. Therefore, stronger interactions (i.e., adhesion forces) correlate with more hydrophobic samples.

## 8. Analytical Model for WCA Modulation by Doping

The Young-Lippmann equation for pure electrowetting can be written as<sup>35</sup>

$$\cos \theta = \cos \theta_0 + \frac{C}{2\gamma} V^2 \dots\dots\dots(1)$$

where  $\theta$  is the contact angle after applying the voltage,  $\theta_0$  is the original contact angle before applying the voltage,  $C$  is the total capacitance of the solid-liquid interface,  $V$  is the applied voltage, and  $\gamma$  is the liquid surface tension ( $\sim 72$  mN/m for liquid water at high RH inside the E-SEM chamber<sup>36</sup>).

This equation can be used for graphene electrowetting when a voltage is applied between the water droplet and graphene. For chemically or electrically doped graphene, electric charges accumulate on the graphene surface because of doping and could influence the solid-liquid surface energy according to the Lippmann equation<sup>37</sup>.

For chemically doped graphene, the applied voltage can be replaced by the graphene surface potential  $U$  as follows<sup>37</sup>:

$$\cos \theta = \cos \theta_0 + \frac{C}{2\gamma} U^2 \dots\dots\dots(2)$$

The surface potential for undoped graphene is considered to be zero; thus, here,  $U$  is the difference in the WF between doped and undoped graphene. Equation 2 suggests that the WCA on both the n- and p-doped graphene with the same surface potential  $U$  will be the same because of the  $U^2$  term. However, the interfacial capacitance will not be constant, as for traditional electrowetting. Instead, it varies with the graphene potential, as shown below.

As shown in Fig. S21, the total interfacial capacitance includes the quantum capacitance of graphene  $C_Q$ , the capacitance of the hydrophobic contaminant layer on top of the graphene  $C_C$ , the capacitance of the Helmholtz layer in water  $C_H$ , and the capacitance of the diffuse layer in water  $C_D$ .

The quantum capacitance can be expressed as<sup>38</sup>

$$C_Q = \frac{2e^3 U}{\pi (\hbar v_F)^2} \dots\dots\dots(3)$$

where  $\hbar$  is the reduced Planck's constant  $\hbar = \frac{h}{2\pi}$ ,  $v_F$  is the Fermi velocity,  $e$  is the electron charge, and  $U$  is the graphene potential. Depending on the doping level, the value varies from 0-0.1 F/m<sup>2</sup><sup>38</sup>.

The hydrophobic contaminant capacitance can be expressed as

$$C_C = \frac{\epsilon_0 \epsilon_c}{d} \dots\dots\dots(4)$$

where  $\epsilon_0$  is the vacuum permittivity,  $\epsilon_c$  is the relative static permittivity of the contaminant layer, and  $d$  is the thickness of the contaminant layer. The contaminant thickness is less than 1 nm<sup>29</sup>, and if the relative static permittivity is considered to be similar to that of nanometer-thick PMMA ( $\sim 2$ )<sup>39</sup>,  $C_C$  is  $\sim 0.05$  F/m<sup>2</sup>. This capacitance does not change with the graphene potential.

The capacitance in the Helmholtz (or Stern) layer,  $C_H$ , can be expressed as<sup>40</sup>

$$C_H = \frac{\epsilon_0 \epsilon_w}{d} \dots\dots\dots(5)$$

where  $d$  is the Debye length  $= \sqrt{\frac{\epsilon_0 \epsilon_w k T}{2 c N_A q^2}}$ ,  $\epsilon_w = 80$ ,  $k = 1.38 \times 10^{-23}$  J/K,  $T = 300$  °K,  $q = 1.6 \times 10^{-19}$  C,  $c$  = solution molarity (mol m<sup>-3</sup>) and  $N_A = 6.02 \times 10^{23}$  mol<sup>-1</sup>. For DI water or a very dilute solution ( $c=0.000001$  M),  $d$  is  $\sim 300$  nm according to the above equation. This value of  $d$  results in a small value of  $C_H$  (0.0023 F/m<sup>2</sup>).

The diffuse layer capacitance can be expressed as

$$C_D = zF \sqrt{\frac{2\epsilon_0 \epsilon_w c}{RT}} \cosh \frac{zFU_H}{2RT} \dots\dots\dots(6)$$

where  $F$  (Faraday's constant) and  $R$  (universal gas constant) are constants,  $c$  is the solution concentration,  $z$  is the magnitude of the ionic charge, and  $U_H$  is the potential of the outer Helmholtz plane.  $U_H$  depends on the graphene potential  $U$ . If the solution concentration  $c$  is very small,  $C_D$  will also be small ( $\sim 0.001$  F/m<sup>2</sup>). Both  $C_H$  and  $C_D$  contribute to the double-layer capacitance,  $C_{DL}$ .

However, using simulations and experiments, other researchers have shown that the Stern model is not accurate because it neglects the interfacial dielectric profile of water<sup>41,42</sup>. For a low-concentration solution or pure water, the value of  $C_{DL}$  has been reported to be 0.035 F/m<sup>2</sup><sup>42</sup>.

Because the capacitances are on the same order of magnitude, all three should be considered. For  $C = \frac{1}{\frac{1}{0.1} + \frac{1}{0.05} + \frac{1}{0.035}} = 0.017$  F/m<sup>2</sup> for  $U=0.4$  V,  $\Theta_0=78^\circ$  and  $\gamma = 71.97$

mN/m, the change in the WCA for 400-meV doping according to Equation 2 is  $\sim 1.5^\circ$ . For 700-meV doping, the change in the WCA is  $\sim 4^\circ$ .

However, because the simple analytical equation has limiting assumptions (e.g., the droplet shape [only applicable at the macro-scale], electric fringe fields at the contact line, and linear dielectric properties, and Young-Laplace equation is limited to WCAs near 90°)<sup>43-45</sup>, a thorough experimental and MD simulation study is needed to better understand this phenomenon.

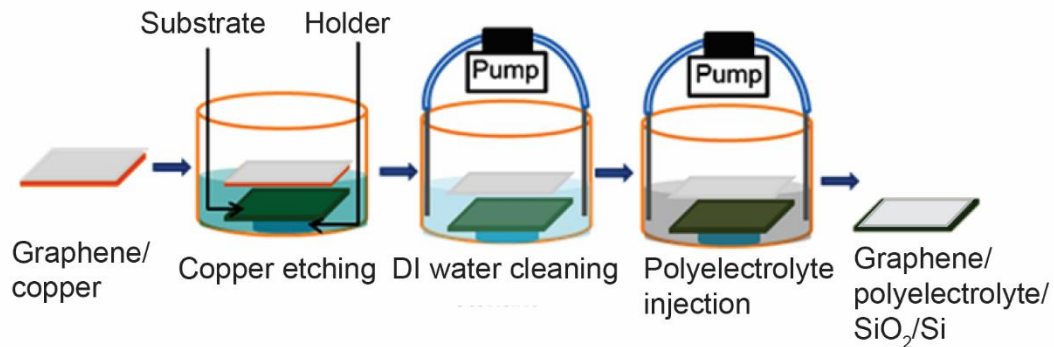


**Figure S1. Transfer method to obtain subsurface polyelectrolyte-doped graphene samples.** A peristaltic pump injects and replaces the etchant solution with DI water to obtain free-standing graphene floating on DI water. After injecting the polyelectrolyte into the water, the same pump is used to lower and place the graphene on top of the SiO<sub>2</sub>/Si substrate, trapping polyelectrolyte in between.

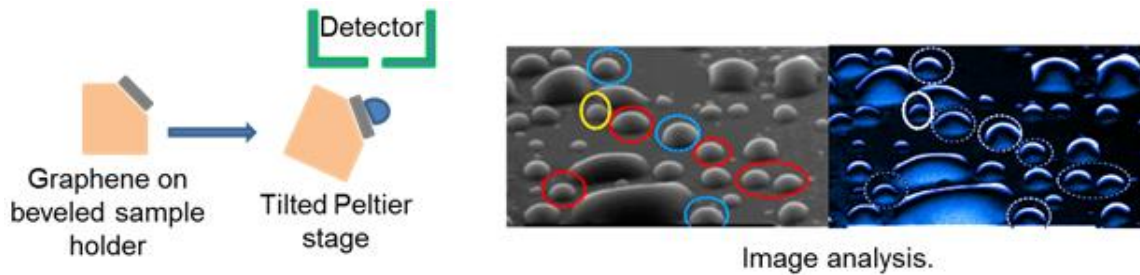


**Figure S2. Schematic illustration showing WCA measurements using E-SEM with a customized beveled sample holder.** Image analysis was conducted using ImageJ software. Red ( $72^\circ$ ), blue ( $79^\circ$ ) and yellow ( $90^\circ$ ) circles indicate water droplets with different WCAs on the same sample, which required defect-free area selection and a statistical analysis of those areas for reliable results.

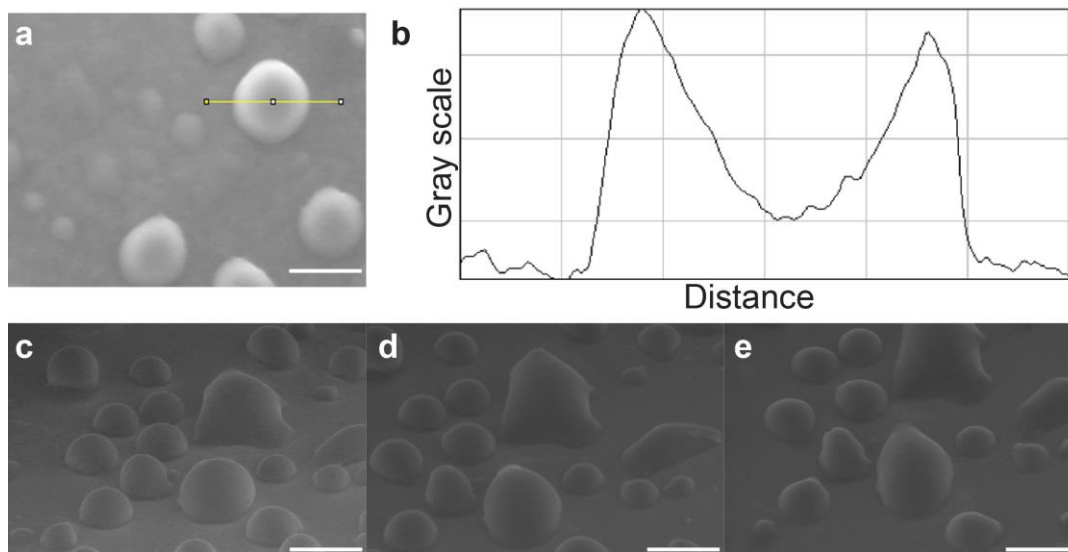


**Figure S3. Effect of inclination angle of the beveled sample holder on the WCA of graphene sample using E-SEM.** E-SEM images captured at 0° (a), 45° (c), 30° (d), and 20° (e). A corresponding intensity map across the yellow line in (a) is shown in (b). WCA was the same in all cases. Scale bars represent 50  $\mu\text{m}$ .

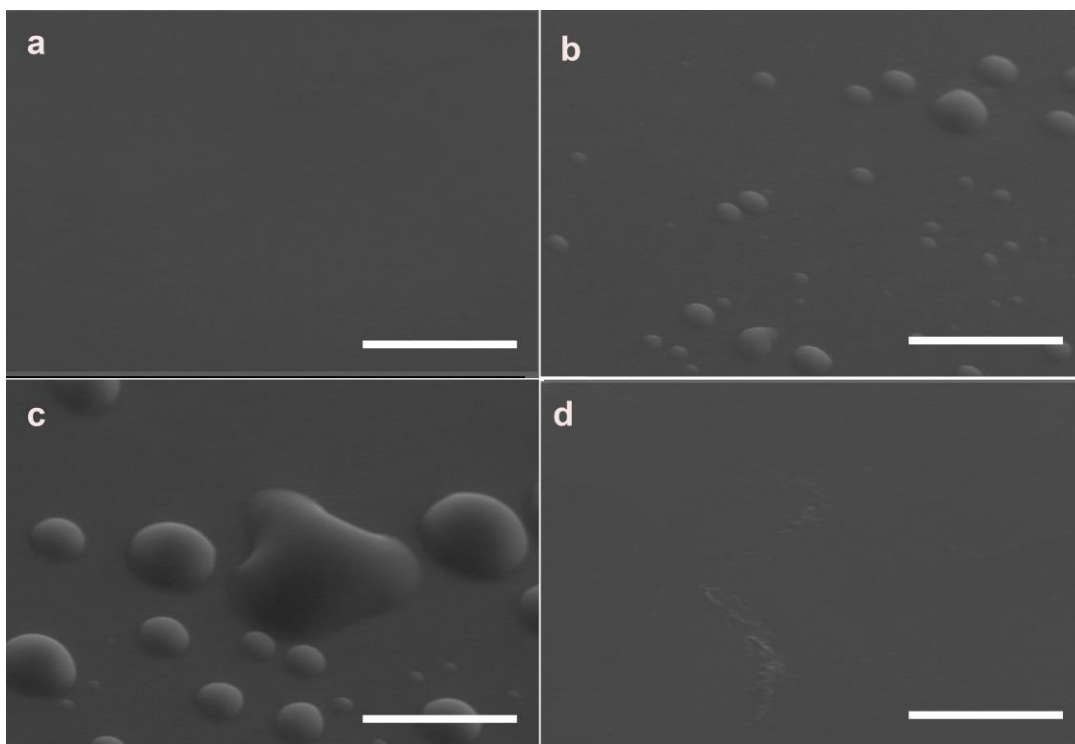


**Figure S4. Progression of E-SEM investigation.** Area selection (a), droplet formation (b), image captured at maximum droplet growth after droplets coalesce (c), and inspection of graphene integrity after WCA measurement (d). Scale bars represent 20  $\mu\text{m}$ .

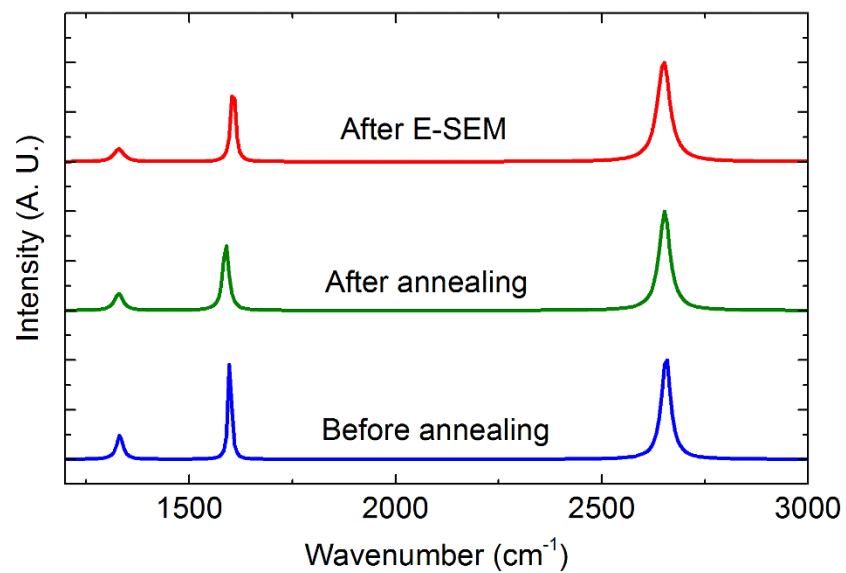


**Figure S5. Raman spectra before and after thermal annealing at 150 °C.** The Raman spectra were the same before and after E-SEM characterizations.

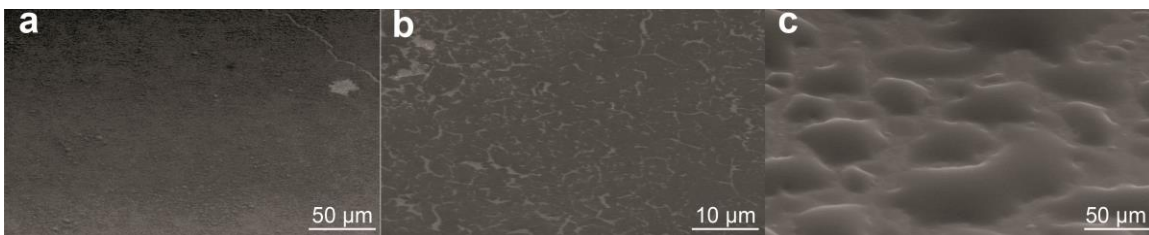


**Figure S6. Effect of broken graphene film on water droplet shape. a,** A surface that appeared smooth at a lower magnification. **b,** Breakage of the graphene film (darker regions) in (a) can be observed at higher magnification. **c,** Water spread on the broken graphene patches in a filmwise manner because of the exposure of the underlying SiO<sub>2</sub> surface.

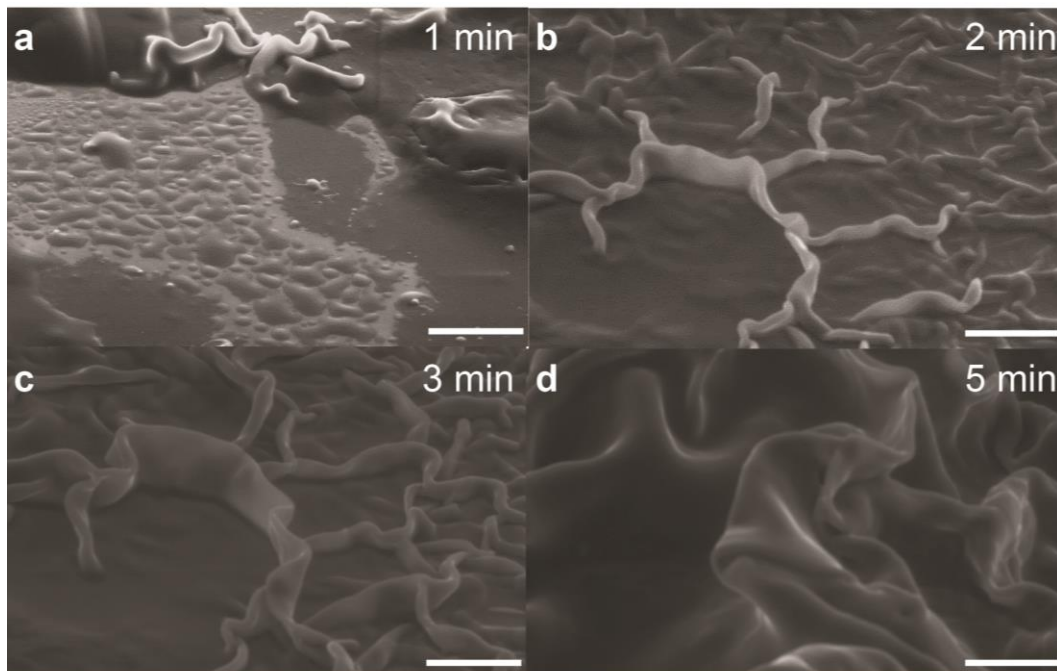


**Figure S7. Polyelectrolyte swelling phenomenon observed using E-SEM.** Broken graphene (darker regions) on HMW PAH was exposed to water vapor at 6.5 mTorr, and images were captured at 1 min (a), 2 min (b), 3 min (c), and 5 min (d) at different spots, showing the swelling of the polyelectrolyte. Scale bars represent 50  $\mu\text{m}$ .

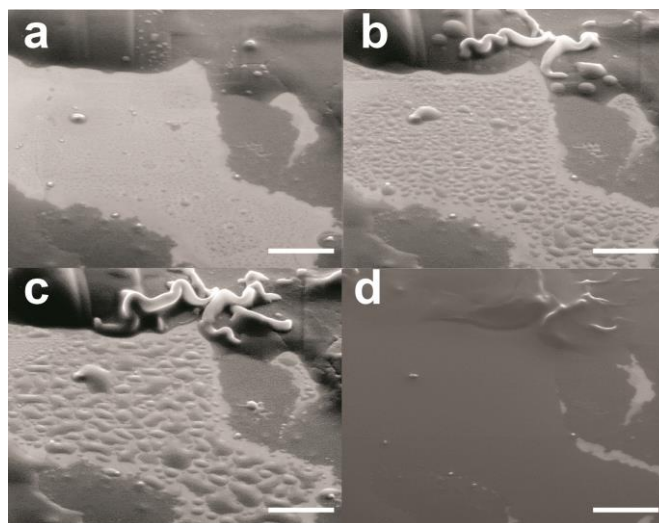


**Figure S8. SEM images showing how graphene can float and move during E-SEM investigation of graphene on polyelectrolyte (HMW PAH) with a large crack.** From (a) to (c), water vapor pressure was increased inside the E-SEM chamber, leading to swelling of the subsurface polyelectrolyte. **d**, Same sample as shown in (a)-(c), but after reducing the water vapor pressure (i.e., drying). Scale bars represent 50  $\mu\text{m}$ .

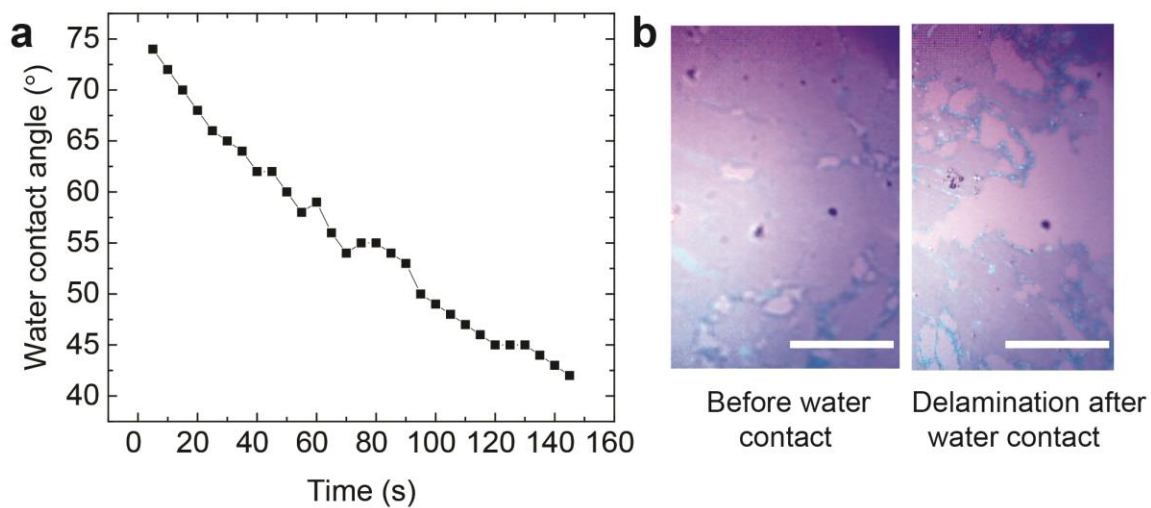


**Figure S9. Macroscopic WCA measurement of graphene.** **a**, Time variation of graphene’s WCA on a polyelectrolyte (HMW PAH)-coated SiO<sub>2</sub>/Si sample measured using a goniometer. **b**, Delamination of graphene on SiO<sub>2</sub>/Si shown by optical microscope images before and after water droplet placement. Scale bars indicate 50 μm.

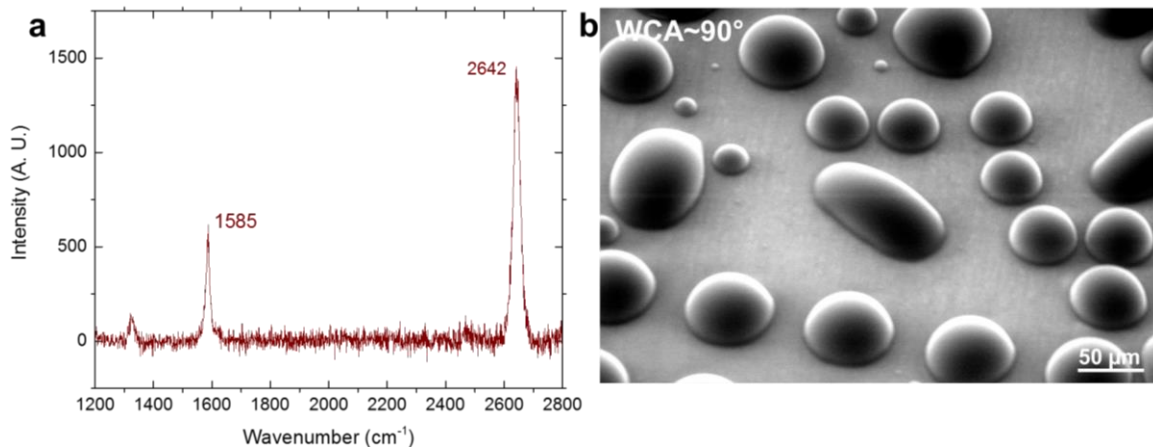


**Figure S10. Comparison with graphene transfer technique utilizing PMMA scaffold.** **a**, Raman spectrum of graphene transferred by PMMA polymeric scaffold with 2D and G band shifted to the left compared to graphene transferred without polymeric scaffold (Fig. 2a) indicating unintentional doping. **b**, WCA measured by E-SEM on graphene transferred by PMMA polymeric scaffold is higher compared to graphene transferred without polymeric scaffold (Fig. 1b) indicating enhanced hydrophobicity due to polymeric residue.

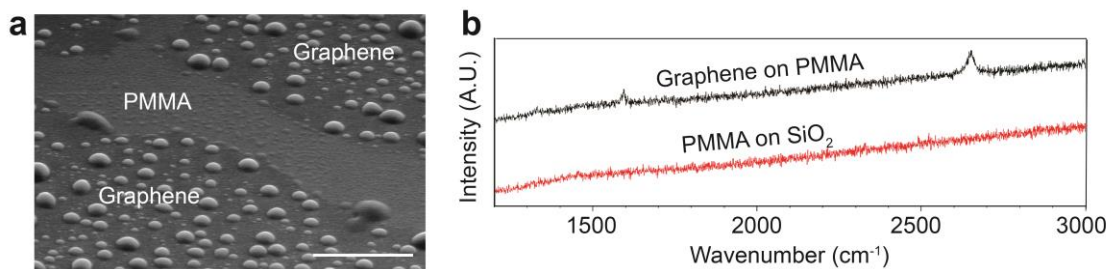


**Figure S11. E-SEM investigation of graphene on PMMA, a polymer without charged groups.** **a**, E-SEM image of water droplets (WCA~80°) on graphene transferred on top of a PMMA thin film on SiO<sub>2</sub>/Si. Scale bar represents 50 μm. Corresponding Raman peaks are shown in **(b)**.

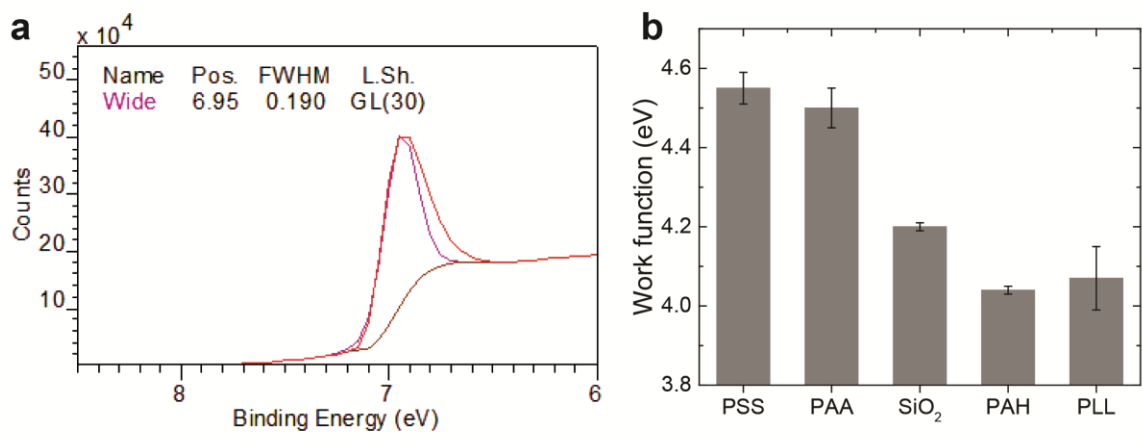


**Figure S12. WF investigation of graphene by UPS. a,** Curve-fitting of UPS raw data to obtain the full width at half maximum (FWHM) and peak positions to determine WF using the equation,  $WF = \text{Photon energy} - (\text{High-binding energy peak position} + \text{Battery voltage} + 0.5 * \text{FWHM} - \text{Offset})$ . A 9-V battery was used for grounding. The instrument offset was calculated using a silver control sample. **b,** WF of polyelectrolyte-doped and undoped graphene samples measured by UPS.

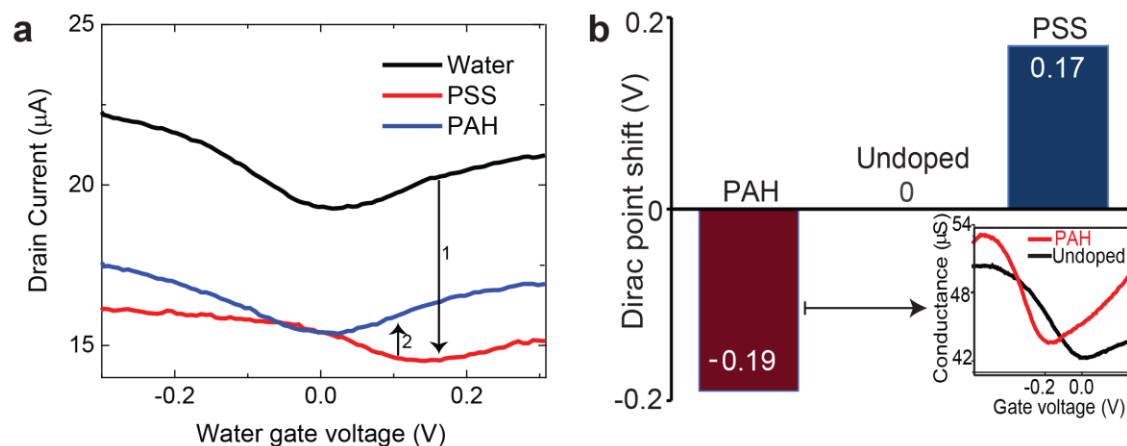


**Figure S13. Investigation of polyelectrolyte solution-induced doping of graphene FET.** **a**, Dirac point shifts in opposite directions were observed when a graphene FET device was solution-gated using two opposite types of polyelectrolyte. After obtaining the DI water-gated (with a Ag/AgCl reference electrode) graphene FET transfer characteristics, we switched to PSS (1) and PAH (2). PSS showed a positive shift of the Dirac point, indicating p-type doping of graphene. The subsequent introduction of PAH resulted in n-type doping behavior of graphene FET. Both polyelectrolytes used were HMW. **b**, Dirac point shifts in opposite directions were observed for n- and p-doping by polyelectrolyte gating of graphene FETs. In this case, different FET devices were used for each polyelectrolyte.

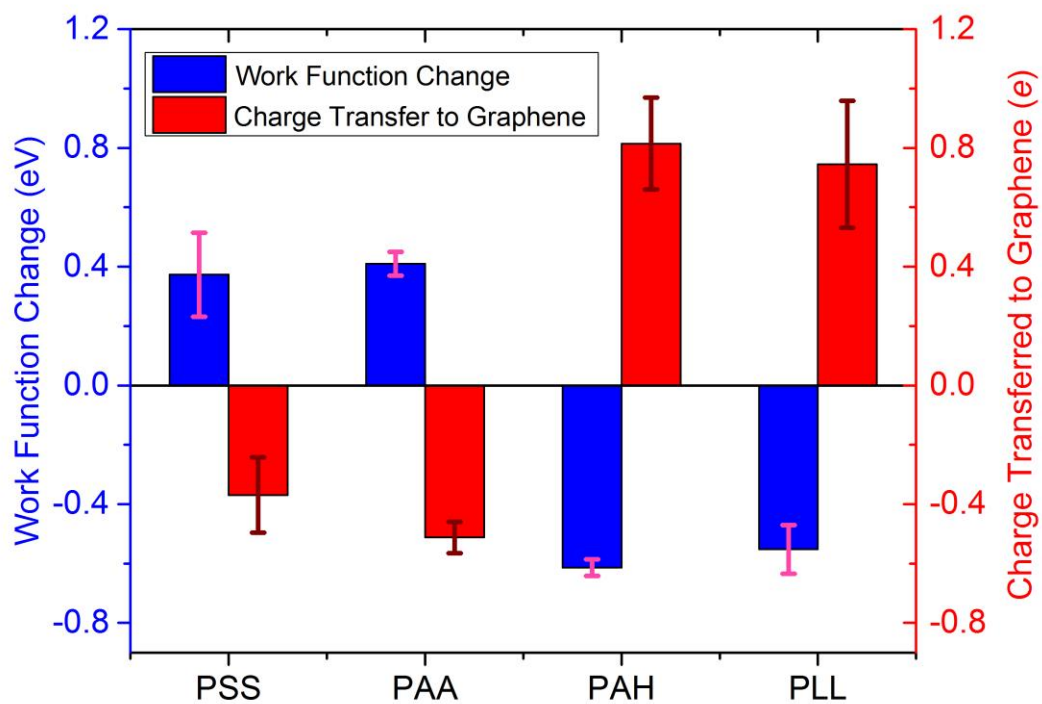


**Figure S14. WF and charge transfer of graphene on various substrates.** A negative Bader population on graphene correlates with charge transfer from graphene to substrates.

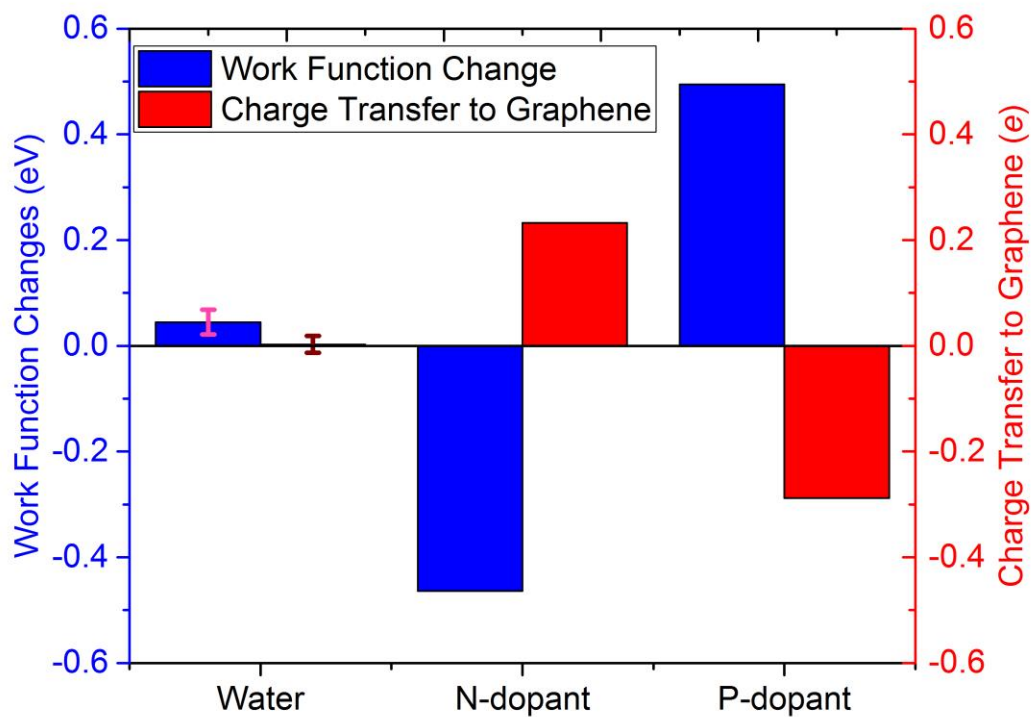


**Figure S15.** WF change of graphene and Bader charge transfer to graphene for water, N-dopant (single boron atom) and P-dopant (single oxygen atom). The results for water were averaged over different water orientations. The shortest distance between water molecules and the graphene surface in all configurations was 2 Å. The distances between both N/P-dopant and the graphene surface were also 2 Å.

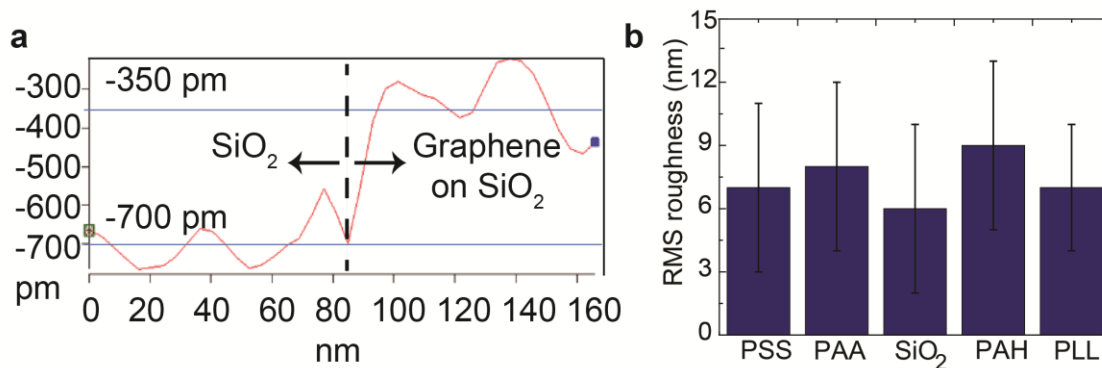


**Figure S16. Graphene layer thickness and topography investigation by AFM. a,** AFM measurement of the layer thickness of graphene on a SiO<sub>2</sub>/Si substrate. **b,** RMS roughness values for doped and undoped graphene samples measured by AFM. The roughness values of the doped and undoped graphene samples were similar. Error bars represent one standard deviation. All polyelectrolytes investigated were HMW.

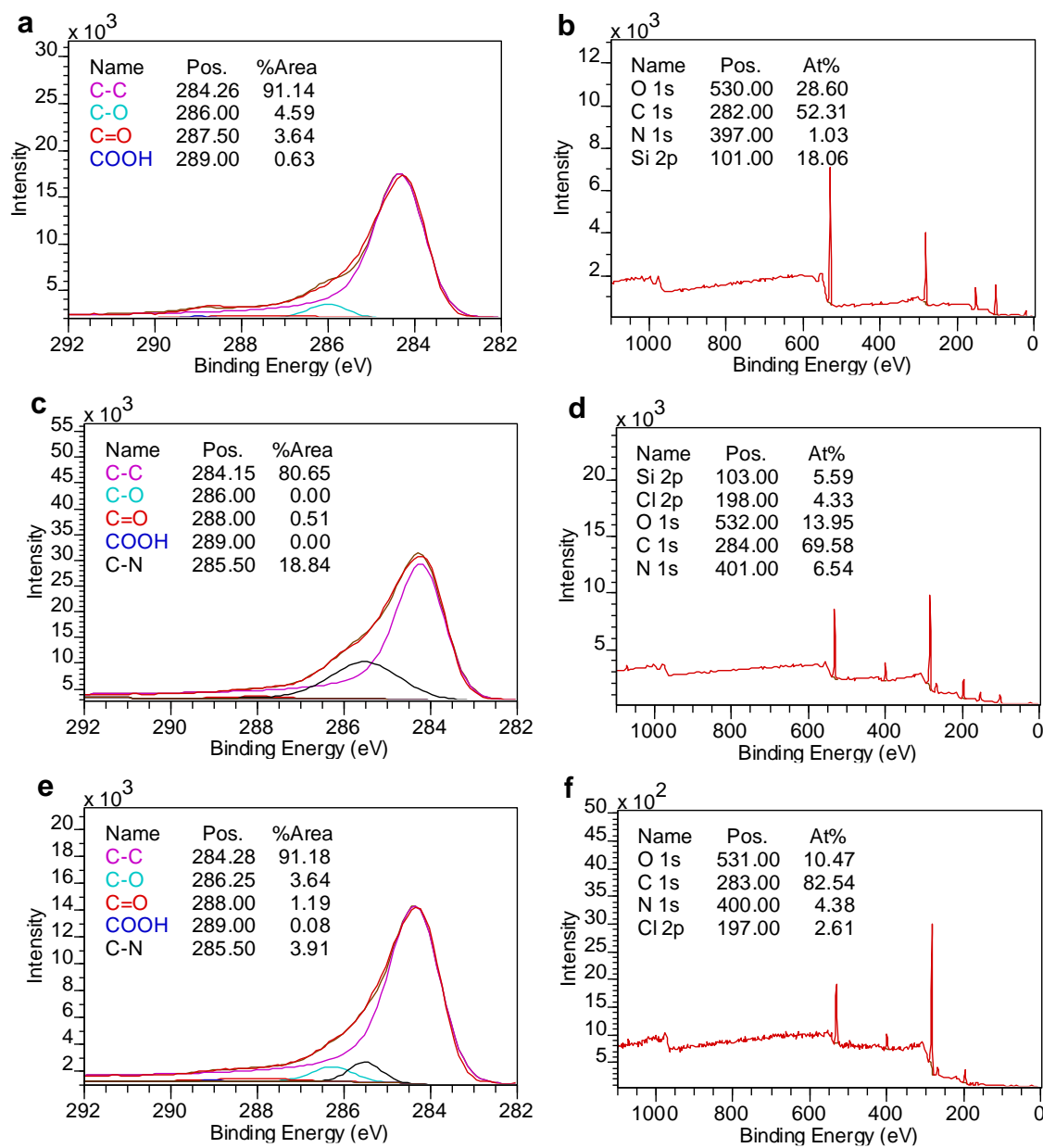


**Figure S17. Investigation of surface functional groups on graphene by XPS.** High-resolution C1s XPS spectra of graphene on SiO<sub>2</sub> (a), graphene on HMW PAH (c) and graphene on HMW PAH at a grazing angle (15°) (e). Survey scan XPS spectra of graphene on SiO<sub>2</sub> (b), graphene on HMW PAH (d) and graphene on HMW PAH at a grazing angle (15°) (f).

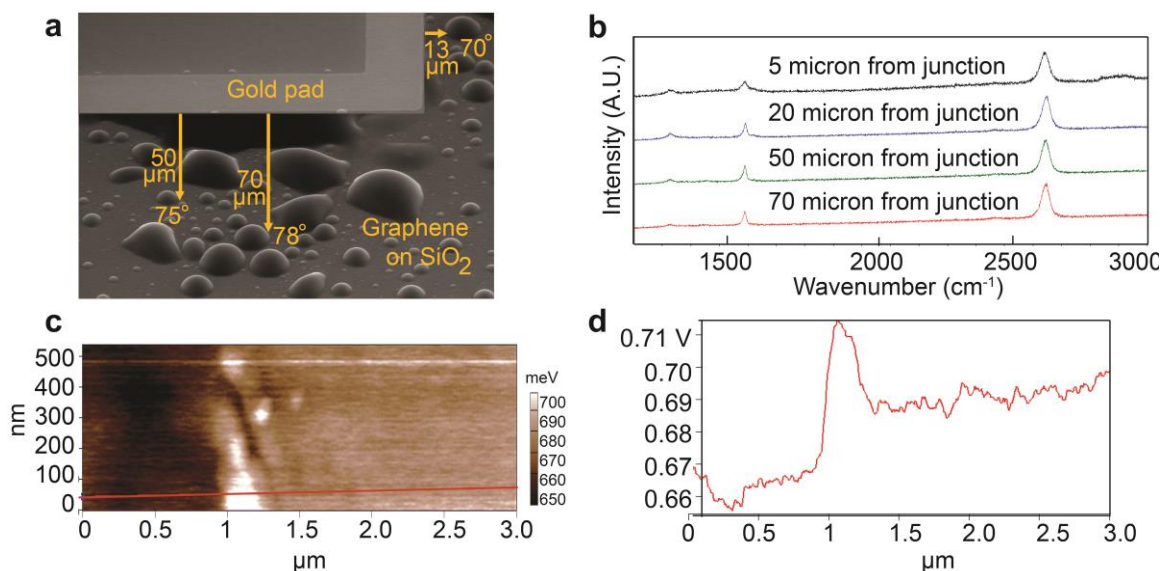


**Figure S18. WCA as a function of distance from the gold-graphene junction.** **a**, ESEM image of water droplets on graphene transferred onto SiO<sub>2</sub>/Si with a lithographically patterned gold pad. The gold pad portion of the image was superimposed from a low-water vapor pressure image to clearly show the gold pad location, which was partially covered by the water film during droplet formation. **b**, The graphene quality was preserved after transfer to the gold, as shown by the Raman data. Raman 2D and G peaks of graphene near the junction (~10-20 μm) is blue shifted by 4-5 cm<sup>-1</sup> and 1-2 cm<sup>-1</sup>, respectively, compared to that of graphene far away from the junction (~70 μm). Therefore, graphene is more p-doped near the junction. This trend is consistent with the observation made for the chemically p-doped graphene samples shown in Fig. 2a. **c**, SKPM map of the graphene surface potential close to the gold-graphene junction. **d**, Surface potential line scan along the red line shown in (c).

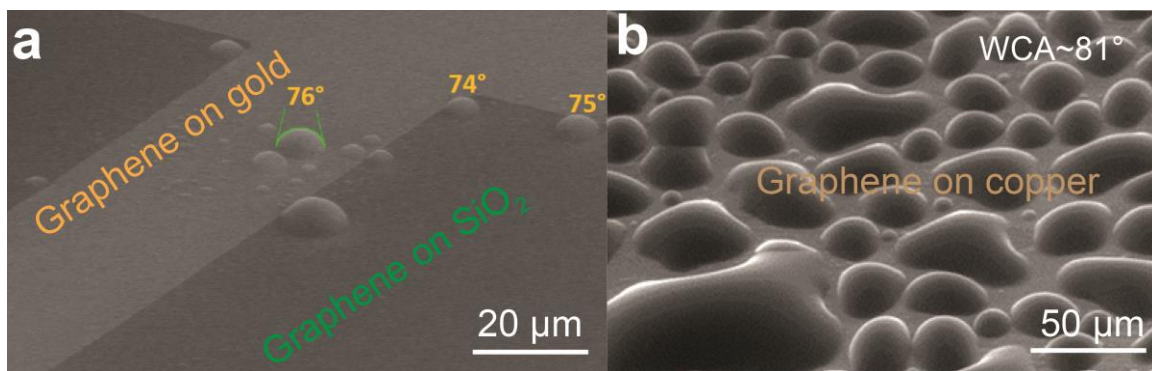


**Figure S19. WCA on graphene sitting on metals.** E-SEM images of water droplets on graphene transferred on top of a gold pad (a) and graphene grown on a polycrystalline copper foil (b).

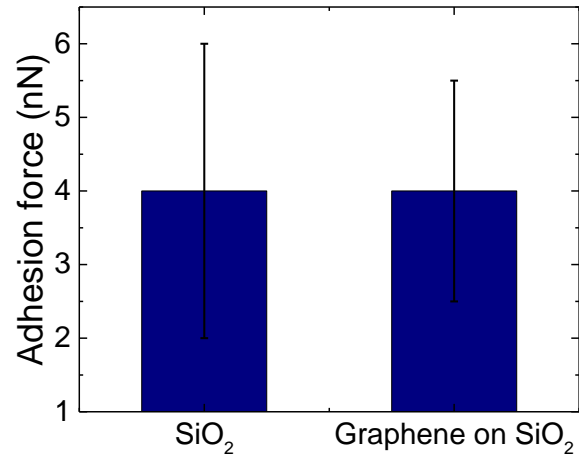


**Figure S20. Control experiment for adhesion force measurement.** The adhesion forces of bare SiO<sub>2</sub> and undoped graphene on SiO<sub>2</sub> were obtained using an uncoated silicon tip with a backside aluminum reflective coating.

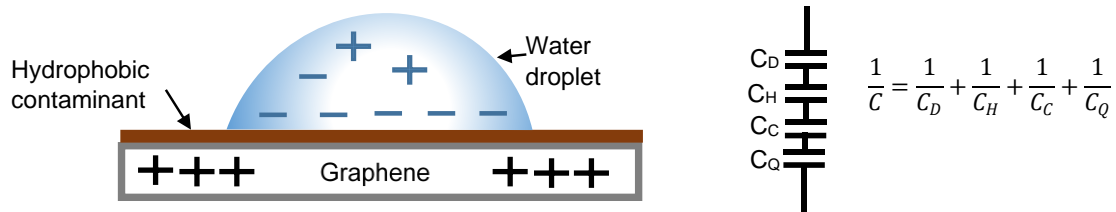


**Figure S21. Graphene-water interfacial capacitances.** Schematic illustration of the various capacitances affecting the chemically doped graphene-water interface.

## Supporting References

- (1) Wang, M. C.; Chun, S.; Han, R. S.; Ashraf, A.; Kang, P.; Nam, S. *Nano Lett.* **2015**, *15* (3), 1829–1835.
- (2) Ashraf, A.; Wu, Y.; Wang, M. C.; Aluru, N. R.; Dastgheib, S. A.; Nam, S. *Langmuir* **2014**, *30* (43), 12827–12836.
- (3) Wang, Y. Y.; Burke, P. J. *Nano Res.* **2014**, *7* (11), 1650–1658.
- (4) Méndez-Vilas, A.; Jódar-Reyes, A. B.; González-Martín, M. L. *small* **2009**, *5* (12), 1366–1390.
- (5) Schneider, C. A.; Rasband, W. S.; Eliceiri, K. W. *Nat. Methods* **2012**, *9* (7), 671–675.
- (6) Stalder, A. F.; Melchior, T.; Müller, M.; Sage, D.; Blu, T.; Unser, M. *Colloids Surfaces A Physicochem. Eng. Asp.* **2010**, *364* (1), 72–81.
- (7) Buron, J. D.; Petersen, D. H.; Bøggild, P.; Cooke, D. G.; Hilke, M.; Sun, J.; Whiteway, E.; Nielsen, P. F.; Hansen, O.; Yurgens, A.; others. *Nano Lett.* **2012**, *12* (10), 5074–5081.
- (8) Flater, E. E.; Ashurst, W. R.; Carpick, R. W. *Langmuir* **2007**, *23* (18), 9242–9252.
- (9) Kresse, G.; Furthmüller, J. *Phys. Rev. B* **1996**, *54* (16), 11169.
- (10) Perdew, J. P.; Burke, K.; Ernzerhof, M. *Phys. Rev. Lett.* **1996**, *77* (18), 3865.
- (11) Neugebauer, J.; Scheffler, M. *Phys. Rev. B* **1992**, *46* (24), 16067.
- (12) Ma, J.; Michaelides, A.; Alfe, D.; Schimka, L.; Kresse, G.; Wang, E. *Phys. Rev. B* **2011**, *84* (3), 33402.
- (13) Harl, J.; Schimka, L.; Kresse, G. *Phys. Rev. B - Condens. Matter Mater. Phys.* **2010**, *81* (11), 115126.
- (14) Jorgensen, W. L.; Chandrasekhar, J.; Madura, J. D.; Impey, R. W.; Klein, M. L. *J. Chem. Phys.* **1983**, *79* (2), 926.
- (15) Werder, T.; Walther, J. H.; Jaffe, R. L.; Halicioglu, T.; Koumoutsakos, P. *J. Phys. Chem. B* **2003**, *107*, 1345–1352.
- (16) Hess, B.; Kutzner, C.; Van Der Spoel, D.; Lindahl, E. *J. Chem. Theory Comput.* **2008**, *4* (3), 435–447.
- (17) Hockney, R. W.; Goel, S. P.; Eastwood, J. W. *J. Comput. Phys.* **1974**, *14* (2), 148–158.
- (18) Nosé, S. *J. Chem. Phys.* **1984**, *81* (1), 511.
- (19) Hoover, W. G. *Phys. Rev. A* **1985**, *31* (3), 1695–1697.
- (20) Romero, H. E.; Shen, N.; Joshi, P.; Gutierrez, H. R.; Tadigadapa, S. A.; Sofo, J. O.; Eklund, P. C. *ACS Nano* **2008**, *2* (10), 2037–2044.

- (21) Ryu, S.; Liu, L.; Berciaud, S.; Yu, Y.-J.; Liu, H.; Kim, P.; Flynn, G. W.; Brus, L. *E. Nano Lett.* **2010**, *10* (12), 4944–4951.
- (22) Ni, Z. H.; Wang, H. M.; Luo, Z. Q.; Wang, Y. Y.; Yu, T.; Wu, Y. H.; Shen, Z. X. *J. Raman Spectrosc.* **2010**, *41* (5), 479–483.
- (23) Iwasaki, T.; Sun, J.; Kanetake, N.; Chikuba, T.; Akabori, M.; Muruganathan, M.; Mizuta, H. *Appl. Phys. Express* **2015**, *8* (1), 15101.
- (24) Tang, W.; Sanville, E.; Henkelman, G. *J. Phys. Condens. Matter* **2009**, *21* (8), 84204.
- (25) Sanville, E.; Kenny, S. D.; Smith, R.; Henkelman, G. *J. Comput. Chem.* **2007**, *28* (5), 899–908.
- (26) Henkelman, G.; Arnaldsson, A.; Jónsson, H. *Comput. Mater. Sci.* **2006**, *36* (3), 354–360.
- (27) Bader, R. F. W. In vol. **22** of *International Series of Monographs on Chemistry*, Oxford University Press Inc., New York, ed. 1, **1990**.
- (28) Fadley, C. S. *Prog. Surf. Sci.* **1984**, *16* (3), 275–388.
- (29) Kozbial, A.; Gong, X.; Liu, H.; Li, L. *Langmuir* **2015**, *31* (30), 8429–8435.
- (30) Yu, Y. J.; Zhao, Y.; Ryu, S.; Brus, L. E.; Kim, K. S.; Kim, P. *Nano Lett.* **2009**, *9* (10), 3430–3434.
- (31) Song, S. M.; Park, J. K.; Sul, O. J.; Cho, B. J. *Nano Lett.* **2012**, *12* (8), 3887–3892.
- (32) Gierz, I.; Riedl, C.; Starke, U.; Ast, C. R.; Kern, K. *Nano Lett.* **2008**, *8* (12), 4603–4607.
- (33) Giovannetti, G.; Khomyakov, P. A.; Brocks, G.; Karpan, V. M.; den Brink, J.; Kelly, P. J. *Phys. Rev. Lett.* **2008**, *101* (2), 26803.
- (34) Amadei, C. A.; Lai, C.-Y.; Esplandiu, M. J.; Alzina, F.; Vecitis, C. D.; Verdaguer, A.; Chiesa, M. *RSC Adv.* **2015**, *5* (49), 39532–39538.
- (35) Arscott, S. *Sci. Rep.* **2011**, *1*, 184.
- (36) Pérez-Díaz, J. L.; Álvarez-Valenzuela, M. A.; García-Prada, J. C. *J. Colloid Interface Sci.* **2012**, *381* (1), 180–182.
- (37) Horiuchi, H.; Nikolov, A.; Wasan, D. T. *J. Colloid Interface Sci.* **2012**, *385* (1), 218–224.
- (38) Xia, J.; Chen, F.; Li, J.; Tao, N. *Nat. Nanotechnol.* **2009**, *4* (8), 505–509.
- (39) Sathish, S.; Shekar, B. C. *J. Optoelectron. Adv. Mater.* **2013**, *15* (3-4), 139–144.
- (40) Velikonja, A.; Gongadze, E.; Kralj-Iglic, V.; Iglic, A. *Int. J. Electrochem. Sci.* **2014**, *9*, 5885–5894.
- (41) Bonthuis, D. J.; Gekle, S.; Netz, R. R. *Phys. Rev. Lett.* **2011**, *107* (16), 166102.
- (42) Nagy, G.; Heinzinger, K.; Spohr, E. *Faraday Discuss.* **1992**, *94*, 307–315.

- (43) Chamakos, N. T.; Kavousanakis, M. E.; Papathanasiou, A. G. *Langmuir* **2014**, *30* (16), 4662–4670.
- (44) Kang, K. H. *Langmuir* **2002**, *18* (26), 10318–10322.
- (45) Mugele, F. *Soft Matter* **2009**, *5* (18), 3377–3384.